LAWRENCE
LIVERMORE
NATIONAL
LABORATORY

LLNL-JRNL-665276

Validating Hydrodynamic Growth in National Ignition Facility Implosions

J. L. Peterson, D. T. Casey, O. A. Hurricane, K. S. Raman, H. F. Robey, V. A. Smalyuk

December 10, 2014

Physics of Plasmas

Disclaimer

This document was prepared as an account of work sponsored by an agency of the United States government. Neither the United States government nor Lawrence Livermore National Security, LLC, nor any of their employees makes any warranty, expressed or implied, or assumes any legal liability or responsibility for the accuracy, completeness, or usefulness of any information, apparatus, product, or process disclosed, or represents that its use would not infringe privately owned rights. Reference herein to any specific commercial product, process, or service by trade name, trademark, manufacturer, or otherwise does not necessarily constitute or imply its endorsement, recommendation, or favoring by the United States government or Lawrence Livermore National Security, LLC. The views and opinions of authors expressed herein do not necessarily state or reflect those of the United States government or Lawrence Livermore National Security, LLC, and shall not be used for advertising or product endorsement purposes.

Validating Hydrodynamic Growth in National Ignition Facility Implosions

J. L. Peterson,[1, a)] D. T. Casey,[1] O. A. Hurricane,[1] K. S. Raman,[1] H. F. Robey,[1] and V. A. Smalyuk[1]
Lawrence Livermore National Laboratory, Livermore, California 94550, USA

(Dated: 19 November 2014)

We present new hydrodynamic growth experiments at the National Ignition Facility, which extend previous measurements up to Legendre mode 160 and convergence ratio 4, thereby completing the growth factor dispersion curve comparison of the low foot and high foot pulses reported by D. T. Casey *et al.* [Phys. Rev. E. **90**, 011102(R) (2014)]. We show that the high foot pulse has lower growth factor and lower growth rate than the low foot pulse. Using novel on-capsule fiducial markers, we observe that mode 160 inverts sign (changes phase) for the high foot pulse, evidence of Richtmyer-Meshkov:Rayleigh-Taylor instability coupling in a spherically convergent system. Post-shot simulations are consistent with the experimental measurements for all but the shortest wavelength perturbations, reinforcing the validity of radiation hydrodynamic simulations of ablation front growth in inertial confinement fusion capsules.

I. INTRODUCTION

Inertial confinement fusion (ICF) energy gain requires the compression and heating of spherical deuterium-tritium (DT) to thermonuclear conditions by intense radiation[1]. In indirectly driven implosions at the National Ignition Facility (NIF)[2], a 1-mm spherical capsule (of plastic[3], beryllium[4] or high density carbon[5]) containing cryogenic DT ice and gas is placed in a cylindrical cavity, or *hohlraum*. NIF's 192 laser beams enter and strike the inner wall of the *hohlraum*, which heats up and bathes the capsule in x-ray radiation. As the capsule surface ablates, it implodes and the centrally confined DT heats to thermonuclear conditions. The goal is ignition: the creation of a thermonuclear burn wave that propagates throughout the DT fuel and produces megajoules of fusion energy.

However, achieving ignition requires careful control of the implosion. The central hotspot must remain largely spherical[6], and the surrounding dense DT fuel shell (which provides inertial tamping for the hotspot) must remain intact and close to Fermi-degenerate during compression[7].

Hydrodynamic instabilities can also threaten ignition, because during an ICF implosion, capsule surface imperfections can become unstable and grow[8,9]. Should these imperfections grow inward towards the capsule center, they can prevent ignition by mixing cold fuel or ablator material into the forming hotspot, or by breaking it apart entirely[10]. As such, the control of hydrodynamic instabilities is one of the critical physics issues for ICF. In particular, ICF implosions are thought to be susceptible to the Richtmyer-Meshkov[11,12] (RM), Rayleigh-Taylor[13,14] (RT) and Kelvin-Helmholtz[15,16] (KH) instabilities. As such, ICF experiments are good laboratories for the study of interacting hydrodynamic instabilities.

In a typical implosion, a carefully shaped x-ray drive shocks the capsule multiple times before accelerating it to high velocity[8]. As the shocks rebound off the capsule center, they meet the incoming dense shell and decelerate it. Numerical simulations and analytic theories predict that shocking subjects the capsule to RM growth[17]. During the main acceleration phase, the outer ablation surface can experience RT growth[18], as does the inner surface during deceleration[19]. RM and RT-driven shear flows can drive the KH instability. Furthermore, as the capsule converges, Bell-Plesset[20,21] (BP) effects can amplify perturbations. Prior to deceleration, simulated growth agrees well with linear analytic theory[22], which can transition to nonlinearity during the late-time stagnation phase[23,24].

Numeric simulation and analytic theory say that shock-induced RM growth serves as the seed for RT growth[22]. The RM seed can have an arbitrary phase: surface bumps can grow outward (with a positive phase) or inward (with a negative phase). RT growth then amplifies the seed perturbation, stretching its amplitude to be either more positive or more negative. Perturbations that grow inward and penetrate the dense shell prior to deceleration tend to be more threatening, because they deposit more ablator and cold fuel into the forming hotspot than do outward going perturbations.

Validating this hydrodynamic growth process in ICF implosions is the goal of the Hydro Growth Radiography (HGR) experiments[25–27]. Simulating hydrodynamic growth can be challenging, especially if perturbations wavelengths are small (high mode number) and if the capsule converges to high convergence ratio ($C_r \doteq R_0/R$). Although growth in ICF implosions comes from (potentially) unknown seeds, beginning as linear growth and then transitioning to nonlinearity, the aim of the initial HGR experiments is to validate the behavior of the simplest system: the nearly linear growth of known seed perturbations during acceleration. Since even this process could involve the coupling of different instabilities, it is still a useful stress test of radiation hydrodynamic simulations.

The first HGR experiments[25–27] examined the growth of pre-imposed Legendre mode perturbations 30, 60 and 90 at $C_r < 2.5$ for two different laser pulses: a "low-foot"

[a)] peterson76@llnl.gov

drive used during the National Ignition Campaign[28] and the "high-foot" drive[29,30] that compresses the fuel less adiabatically (a "higher adiabat" implosion) in exchange for increased ablation front RT stability. These experiments measured that surface perturbations grew less with the high-foot pulse than with the low-foot pulse, in agreement with simulations. No evidence was found of modal phase-inversion (all modes had positive phase), and the measured growth appeared to be decreasing at higher mode number, as expected from the ablative stabilization[18] of higher mode number perturbations.

A few questions remained after these initial experiments. Does the growth of higher modes actually decrease, as predicted, or is ablative stabilization weaker than expected? Does the agreement with simulations continue as the capsule converges to smaller radii? Does RM actually seed RT growth in converging systems, as demonstrated by different modes with different phases?

This paper reports on a series of shots designed to address these questions. In particular, our HGR experiments extend the low-foot:high-foot comparison to higher mode number (up to Legendre mode 160) and higher convergence ratio (up to 4). In essence, we find that the agreement between simulation and experiment continues, that the growth of higher modes is indeed less than lower modes, and that phase inversion is possible in converging systems. We find that the both the growth factor and growth rate of the high-foot pulse is less than the low-foot pulse, and that while all modes have positive phase for the low-foot pulse, mode 160 inverts phase for the high-foot pulse. Together, these data provide evidence that both the RM and RT instabilities are different for the high-foot and low-foot pulses.

The remainder of this paper is outlined as follows. We review the HGR experimental platform in Section II. Section III describes the higher convergence ratio shot, N140127, and Section IV describes the higher mode number shots, N140131 and N140313. The new data are discussed in the context of the previous HGR experiments in Section V, and we conclude in Section VI.

II. THE HYDRO GROWTH RADIOGRAPHY (HGR) EXPERIMENTS

The NIF HGR platform[25–27] allows for the single-pass radiographic measurements of capsule perturbations. An ignition-scale capsule sits on a re-entrant cone, as in shock-timing VISAR "keyhole" experiments. The surface of the capsule is machined with pre-imposed two-dimensional perturbations of specified Legendre mode and amplitude. As the capsule implodes, the perturbation grows. Eight of the 192 NIF laser beams are directed onto a backlighter foil, which emits x rays that pass through the cone and the capsule, and a framing camera captures images at four distinct times. The framing camera records pinhole and slit-averaged images of x-ray transmission through the capsule, as well as through a strip of aluminum, to determine the absolute energy of the emitted x rays. The growth of the perturbation is characterized by the optical depth modulation and wavelength, which is directly proportional to the capsule radius. The optical depth κ is related to the transmission T by $\kappa = -\ln T$, so that a larger value coincides with more attenuation, as expected from x rays passing through more material.

The measured radiographic images are compared against synthetic radiographs, post-processed from two-dimensional capsule-only HYDRA[31,32] simulations of the experiment, which are run in either a "pre-shot" or "post-shot" mode. All simulations use the measured capsule surface perturbation and dimensions, but post-shot simulations include adjustments the radiation source drives due to as-fired laser power fluctuations. Notionally, the low-foot and high-foot pulses are the same as in the previous HGR studies[25–27], as are the experimental and computational setups. However, our higher convergence experiment (N140127) used an Fe backlighter (6.8 keV) to image at smaller radii (and higher optical density), and our higher mode number experiments (N140131 and N140313) used a Sc backlighter (4.5 keV) and a 12 μm slit, to better resolve the smaller wavelengths. Furthermore, our simulations are run at a higher resolution (roughly 700 radial zones and at least 100 angular zones per perturbation wavelength, corresponding to roughly 2x radial and 3x angular resolution); a convergence study showed that this resolution is accurate to ten percent. For additional details on the HGR platform and analysis, see Ref. [26].

III. HIGHER CONVERGENCE EXPERIMENT

The goal of NIF shot N140127 was to extend the HGR measurement to $C_r > 4$, near the time of peak implosion velocity and the end of the acceleration phase. Of particular interest was whether or not the agreement reported between simulation and experiment at $C_r \approx 2$ would continue to smaller radii, or whether the simulated and measured growth would diverge. For a few reasons, the high foot pulse and a mode 30 perturbation (with initial amplitude 0.85 μm) were chosen for this task. Firstly, with its lower growth, the high foot pulse's growth was more likely to remain nearly linear later in time. Secondly, mode 30's larger wavelength is more easily resolved at small radii. Additionally, Fe was used a backlighter (instead of V) to get a better signal as the capsule shell densifies.

Figure 1a shows the measured (square) and simulated (triangle with lines) optical depth modulation amplitudes and wavelengths from the four radiograph times. Uncertainties are represented by dashed ellipses. Since wavelength is a measure of capsule radius, time moves from right to left. The simulations agree with the experiments (given the uncertainties) at a fixed wavelength. That is, at a particular radius, the optical depth modulations

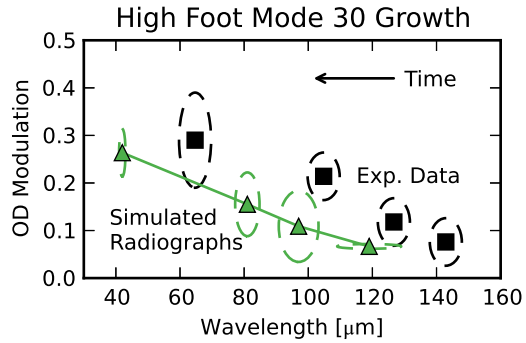

(a) Optical depth modulation amplitude as a function of wavelength.

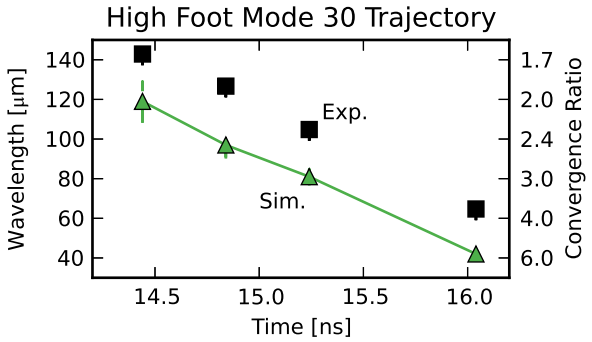

(b) Modulation wavelength and inferred convergence ratio as a function of time.

FIG. 1. Comparison of simulated (triangles) and measured (squares) radiographs for the high foot mode 30 experiment, N140127. Dashes represent uncertainties.

overlap; there is no divergence between simulation and experiment at the smallest radii. However, although the radiographs are taken at the same times in the experiment and simulation, the wavelengths do not agree. This indicates that the simulation and experiment do not have the same trajectory, because at a particular time, the simulated radiograph is at smaller wavelength (and therefore smaller radius) than that of the experiment. This phenomenon is clearly shown in Fig. 1b, the wavelength (and convergence ratio) from each radiograph as a function of time. The experiment measures up to $C_r \simeq 4$, but the simulation runs to $C_r \simeq 6$. Clearly, the simulation has moved ahead of the experiment.

A possible explanation for this behavior is the uncertainty in the simulated drive spectrum. Post-shot drive spectra are adjusted[33] to match early time shock velocity measurements and late time capsule trajectories and x-ray bang times. This process introduces some uncertainty in the magnitude and spectral content of the radiation drive seen by the capsule. As mentioned in Ref. [26], the uncertainty on the >1.8 keV ("m-band") part of the spectrum is roughly 30%. Figure 2 shows the effects of

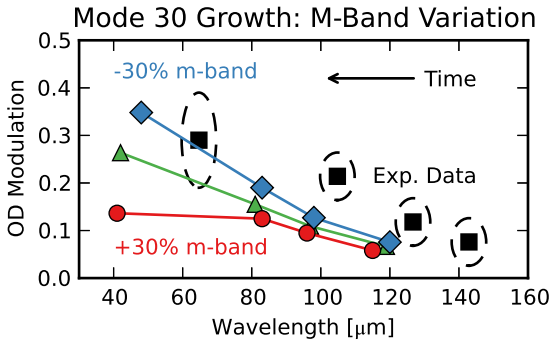

FIG. 2. Sensitivity of N140127 simulated radiographs to m-band drive content (>1.8 keV). Points are from radiographs taken at the same time as in the experiment.

this variation on the simulated optical depth modulation amplitude and wavelength. Decreasing the m-band increases the growth, so that a 30% variability in m-band corresponds to roughly a 30% variability in simulated amplitude. This sensitivity is much greater than that due to opacity or equation of state, in particular because these variables are highly constrained by early time shock measurements. Changing the equation of state changes not only the growth, but also shock trajectories. Readjusting the drive back to consistency with shock timing measurements moves the calculated growth back towards its original value, so that the variability in amplitude due to equation of state is less than 10%.

Although the m-band can affect the magnitude of growth, it cannot bring the simulated and measured trajectories into agreement. Lowering the m-band moves the simulation closer to the experiment, but not enough to account for the full difference in measured and simulated wavelengths.

Despite the disagreement in trajectories, the results of N140127 show that the simulated and measured growth of mode 30 are consistent at a given convergence ratio up to $C_r \simeq 4$. An uncertainty in simulated growth of roughly 30% can be attributed to uncertainties in thermal drive spectra.

IV. HIGHER MODE NUMBER EXPERIMENTS

NIF shots N140131 and N140313 aimed to extend the HGR-measured growth to high mode number, to finish the growth factor comparison of the low- and high- foot pulses, and to measure modal phase inversion in a converging geometry.

Phase inversion has been seen in planar RM-RT experiments that use streaked x-ray imaging to time-resolve the evolution of a perturbation[34]. A challenge with observing phase inversion in a converging implosion is that the phase is settled early on, by the RM instability during

the shocking phase, but the capsule accelerates and the perturbations grow much later. For that growth to remain linear, the initial perturbation must be too small to resolve during the RM phase, and as the capsule shell densifies, its optical depth changes so that by the time the signal is diagnosable, the phase is already set. Therefore, following the continuous time-history of the perturbation is difficult, and the phase must be determined from individual snapshots of the perturbation.

The phases of modes 30-90 were previously determined by measuring the growth of two modes side by side and analyzing the connection joint between two different wave number perturbations (see Appendix A in Ref. [26]). However, this analysis relied on both modes growing to large amplitude, so that they could be reliably compared against one another. At higher mode number the growth was anticipated to be much less, and the exact location of the demarcation between positive growth (which is predicted at lower mode numbers) and negative growth (which is predicted at higher mode numbers) was uncertain. The previous phase measurement method required both modes to grow robustly, an unlikely situation at higher mode number.

To avoid the possibility of one mode's growth compromising a phase measurement, the HGR ripples were modified to include on-capsule spatial fiducial markers in the form of two localized perturbations each with twice the depth of their neighboring ripples. These locally deep grooves (known as "Fiducially Aligned Nonlinear Growth Seeds" or "fangs") were placed away from the center perturbation joint, so that they would appear on the edges of the gated camera line-of-sight and not compromise the central measurement. Since locally the fangs represent a departure from a pure Legendre mode, this placement also prevents them from obfuscating the measurement in the center of the capsule. The presence of fangs on a radiograph allows it to be aligned to with the initial perturbation to determine the phase of the growth; because the fangs are locally deeper, the capsule is locally optically thinner, and integer wavelengths away from the center of a fang will align with bright spots if the growth is positive. They will instead be darker if the growth has inverted.

The capsules were each machined with Legendre modes 120 and 160 side-by-side, with an amplitude of 1 μm (2 μm peak-to-valley). One fang was placed for each mode of amplitude 1.5 μm (3 μm peak-to-valley).

Fig. 3 contains the radiographic snapshots of the perturbations' evolution for the two experiments. The images from the low-foot experiment, NIF shot N140131, appear on the left and those of the high-foot experiment, NIF shot N140313, are on the right. Time evolves from top to bottom. Both cases show two distinct wavelengths of different amplitudes. Mode 120 has a larger modulation amplitude than 160 for the low-foot shot, but mode 160 has a larger amplitude for the high-foot shot. By comparing frames from similar radii, it is clear that the high-foot growth is less than the low-foot, consistent

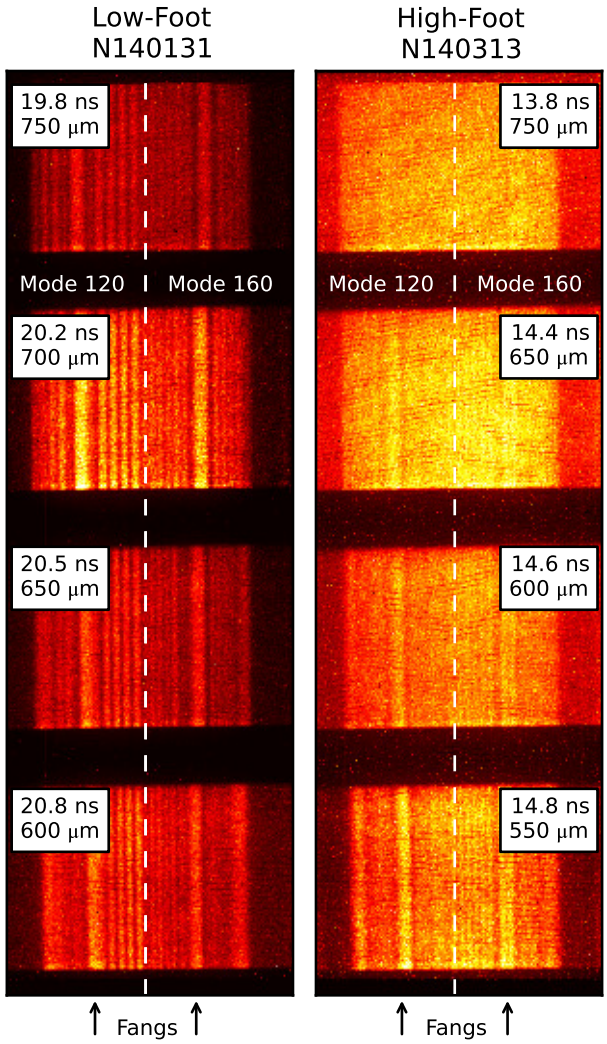

FIG. 3. Slit radiographic images of the two implosions, showing the evolution of modes 120 (on the left half of each image) and 160 (on the right half). The bright bands, marked with arrows, are the on-capsule "fang" fiducial marks that allow for a phase measurement.

with the observations made for modes 30-90. Additionally, each radiograph shows two bright bands that move together as time progresses and the capsule compresses. These are the signatures of the fangs. Figure 4 shows slit-averaged optical depth modulations as calculated from the measured radiographs at 600 μm (image 4 for the low-foot shot and image 3 for the high-foot shot). Additionally, overlaid on each radiographic measurement is an atomic force microscopic trace of each capsule's initial surface perturbation. The signatures of the fangs on the radiographs have been aligned with the fangs on the initial perturbation. Since κ is inversely proportional to measured transmission, large values correspond to regions of greater column density. Both modes for the low-foot are in phase with their initial surface perturbation (dark regions with large κ correspond to peaks

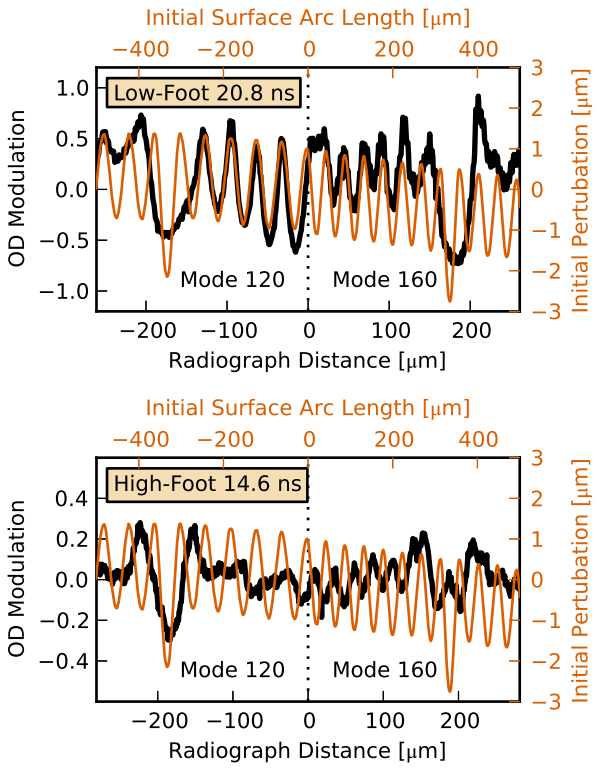

FIG. 4. Slit-averaged optical depth modulation lineouts for the low-foot (top) and the high-foot (bottom) experiments (thick lines; left and bottom axes). Each line out is aligned with the pre-shot measured perturbation (thin lines; right and top axes).

on the initial perturbation). Little signal (beyond the fang mark) appears for the mode 120 high-foot shot, but the mode 160 high-foot growth is clearly out of phase with the initial perturbation. Therefore, mode 160 has inverted phase for the high-foot implosion.

V. DISCUSSION AND COMPARISON WITH PREVIOUS EXPERIMENTS

The measured and simulated optical depth modulation amplitudes for both these and the previous HGR experiments[25–27] appear together in Fig. 5 as a function of capsule radius, as inferred from the measured perturbation wavelengths. Colors correspond to mode number, with the lowest mode 30 as red and the highest mode 160 as purple. Experimental measurements and uncertainties appear as points and simulated values appear as bands, the span of which represents the combined uncertainty due to resolution and m-band.

A few observations are noteworthy. First of all, for both the low foot (left) and high foot (right), the simulations and experiments are consistent, given uncertainties, for all modes except for mode 160. The measured growth from this mode is higher than calculated from post-shot simulations (although the sign is correctly modeled). Secondly, the mismatch in capsule trajectory noted for the mode 30 high foot experiment appears to hold true for all modes, since the radius of the last simulated radiograph (at the left-most end of the simulation bands) does not match the radius of the last measured radiograph (the left-most point for each mode). Indeed it appears that the simulations of the high-foot pulse are all at smaller radii than the experiment. This is not the case with the low foot, as all of the simulations and experiments end at the same radii. A possible explanation is that the thermal part of the high foot tuned drive is too strong, and it may be possible to further constrain the high-foot drive to the HGR measurements. The low-foot drive, however, already appears consistent with the HGR measurements.

It is possible to approximate linear optical depth growth factors by normalizing the measured growth factor to the ratio of the simulated linear growth factor to the simulated post-shot nonlinear growth factor[26]. For these data, this factor is roughly unity for all points, because our experiments were designed to remain nearly linear throughout the measurement time frame. The results of this procedure appear in Fig. 6, experimental linear growth factors as a function of radius and mode number for the low foot and high foot pulses. (For clarity, we have omitted the uncertainty that carries through to this calculation from the simulations.)

For both pulses, mode 60 grows the most, followed by mode 90 for the low foot and mode 30 for the high foot. We show in Fig. 7 the measured and simulated growth factor at a radius of 650 μm, where data for all modes exist. The complete growth factor curves show that the high foot pulse has lower growth than the low foot pulse across the mode spectrum and that the simulations agree with the experiments for all but the highest mode number. As predicted by simulation, the experimental growth factor curves decrease at high modes, behavior that is consistent with the ablative stabilization of RT growth.

Additionally, it is possible to fit the linear growth factor data to exponential growth rates, the results of which are shown in Fig. 8a. However, the growth rates do not appear to be consistent with the growth factors, for instance because the high foot mode 30 appears to be growing more rapidly than that of the low foot.

This discrepancy can be resolved by removing the effects of compressible convergence from the data. The total measured growth is the combination of RT and BP growth. Since the data are taken at different radii, the effects of convergence complicate a fit to the pure exponential growth one expects from the RT instability.

Explicitly, the total growth factor η can be thought of as the product of the exponential RT growth $\eta_{RT} \sim \exp(\gamma t)$ and non-exponential BP growth η_{BP}, which is a function of mode number l and convergence ratio C_r and can be estimated as[21]:

$$\eta_{BP} = C_r^{1/4} \exp\left[\sqrt{2l}\left(\arcsin\sqrt{1-1/C_r} - \sqrt{1-1/C_r}\right)\right] \quad (1)$$

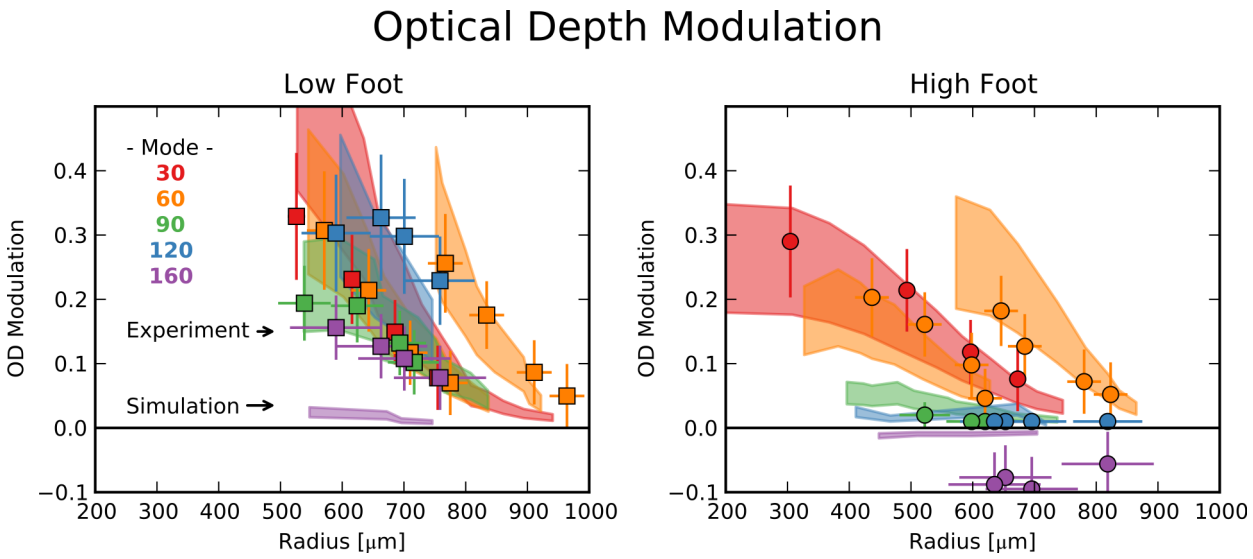

FIG. 5. [Color] Measured (points) and simulated (bands) optical depth modulation amplitude for the low-foot pulse (left) and the high-foot pulse (right), color-coded by mode number. Simulation bands represent uncertainties.

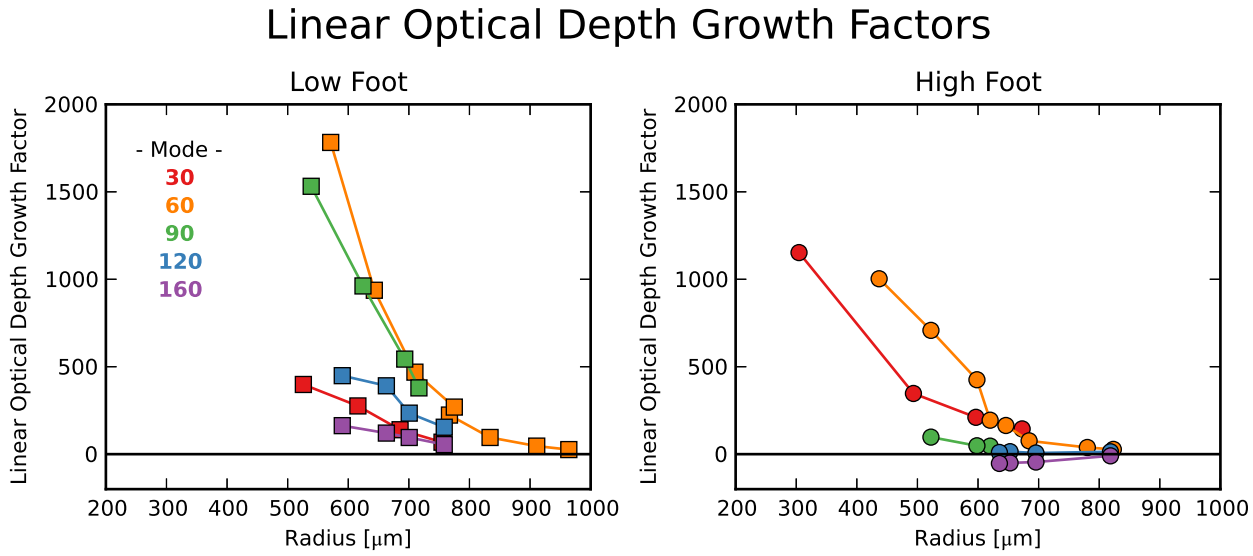

FIG. 6. [Color] Linear optical depth growth factors as a function of radius for the low-foot (left) and high-foot (right), color-coded by mode number.

Normalizing each growth factor data point to the appropriate convergence factor from Eq. 1 and re-fitting to exponential growth gives the growth rates in Fig. 8b. Overall, the growth rate decreases for all modes, for some modes by a factor of two, and the growth rate of higher mode numbers is decreasing towards zero. For both modes 30 and 60, the low foot data grows at a faster rate than the high foot data. At higher modes, the fit uncertainties overlap, so it is difficult to conclude that high foot has lower growth rate at these modes, but mode 60 appears to be growing 20-30% faster in the low foot experiments. Even this small difference is significant. As an example, the growth time for each pulse is roughly 3-3.5 ns. The growth rate of mode 60 is roughly 1.25 ns^{-1} for the low foot and about 1.0 ns^{-1} for the high foot, so that conservatively one expects the ratio of the low to high foot growth factors to be $\simeq \exp(1.25 \times 3)/\exp(1.0 \times 3) = 2.1$. That is, the differences in measured growth rates can account for at least a factor of two difference in growth factor for the low and high foot pulses at fixed convergence ratio.

Not only do the HGR data suggest that the RT instability growth is different for the two pulses, but also that the RM growth seed is different. The two pulses

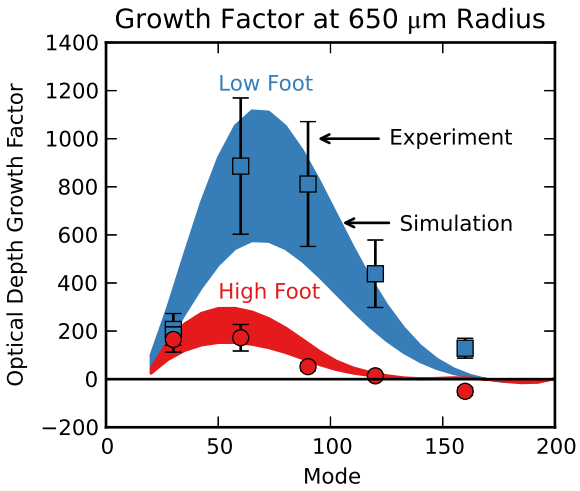

FIG. 7. Optical depth growth factor as a function of Legendre mode number at 650 μm.

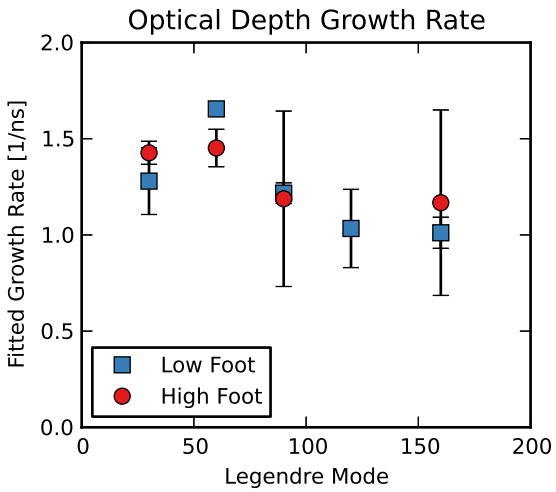

(a) Growth rates from optical depth growth factors.

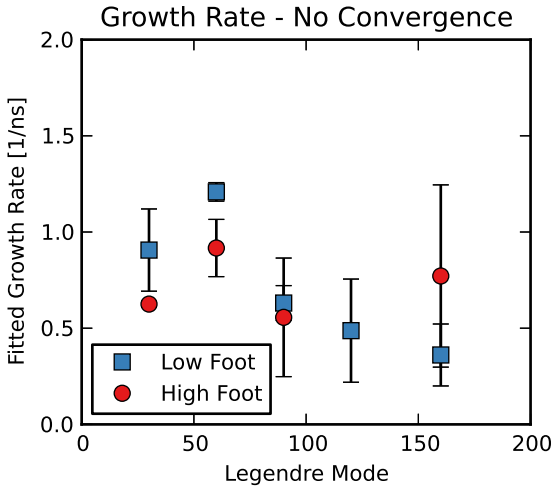

(b) Growth rates from optical depth growth factors with convergence effects removed.

FIG. 8. Growth rates from an exponential fit to experimental linear growth factors for the low foot (squares) and high foot (circles) pulses. Bands are fit uncertainties.

clearly have different zero-phase crossing locations in mode space, since mode 160 was measured to be negative for the high foot, but positive for the low foot. If the sign of the growth depends on RM dynamics, and the measured signs are different, so too must be the RM dynamics. This is not unexpected, since the the high foot pulse has fewer shocks and a stronger first shock, which in particular is predicted to move the demarcation between positive and negative growth to lower mode number[22,35], consistent with the HGR observations.

Taken as a whole, the HGR measurements suggest that the lower growth observed in the high foot pulse comes from a combination of favorable RM and RT dynamics. For the high foot, the RM instability has a zero seed at a lower mode number, closer to the peak of the RT growth rate (which itself is lower), so that the most unstable modes start with lower initial amplitudes and grow at slower rates. The combined effect of RM zero-crossing location and lower RT growth rate leads to a lower overall growth factor for the high foot pulse.

VI. CONCLUSIONS

In conclusion, the HGR experiments on the linear growth of pre-imposed modulations have been extended to $C_r = 4$ and Legendre mode 160, completing the growth factor curve comparison of the low foot and high foot designs. Post-shot simulations agree with experimental measurements, given uncertainties, even at larger convergence ratios, closer to peak implosion velocity, and measured growth factors decrease at higher mode number, as expected from the ablative stabilization of small wavelength perturbations.

The use of novel on-capsule fiducial markers ("fangs") allowed for the unambiguous observation of the modal phase inversion of mode 160 for the high foot pulse, evidence of RM-RT coupling in a spherically convergent ignition-relevant system. The different phase measurements suggests that the RM seed is different for the high and low foot designs, in a manner consistent with theory and simulation, and in a manner that leads to lower initial seed for the high foot. Furthermore, the inferred growth rates of the lower modes suggest that the RT growth is different between the low and high foot pulses, consistent with the observation that the high foot pulse has a longer ablation front scale length[36]. In other words, the HGR measurements of growth rate and mode phase suggest that the lower overall high foot growth comes from a combination of favorable RM and RT dynamics.

Given their consistency with simulations, these experiments serve as bedrock for additional studies on hydrodynamic growth in ignition-relevant implosions. Of particular interest are testing the growth of perturbations on different ablators and measuring the nonlinear growth of unknown "native roughness" capsules (capsules without added perturbations). Finally, HGR experiments can be used to test theories on how to control growth in future designs.

ACKNOWLEDGMENTS

The authors wish to thank the entire NIF and WCI operations and design staff for supporting this work, as well as the LLNL and General Atomics Target Fabrication teams. In particular, we appreciate the help of D. Callahan, D. Clark, S. Haan, D. Hoover, B. Kauffman, J. Kroll, O. Landen, N. Meezan, A. Nikroo and B. Remington. This work was performed under the auspices of the U.S. Department of Energy by Lawrence Livermore National Laboratory under Contract DE-AC52-07NA27344.

[1] J. Lindl, *Inertial Confinement Fusion* (Springer-Verlag, 1998).
[2] G. H. Miller, E. I. Moses, and C. R. Wuest, Nuclear Fusion **44** (2004).
[3] D. S. Clark, S. W. Haan, B. A. Hammel, J. D. Salmonson, D. A. Callahan, and R. P. J. Town, Physics of Plasmas **17**, 052703 (2010).
[4] A. N. Simakov, D. C. Wilson, S. A. Yi, J. L. Kline, D. S. Clark, J. L. Milovich, J. D. Salmonson, and S. H. Batha, Physics of Plasmas **21**, 022701 (2014).
[5] A. J. MacKinnon, N. B. Meezan, J. S. Ross, S. Le Pape, L. Berzak Hopkins, L. Divol, D. Ho, J. Milovich, A. Pak, J. Ralph, T. Döppner, P. K. Patel, C. Thomas, R. Tommasini, S. Haan, A. G. MacPhee, J. McNaney, J. Caggiano, R. Hatarik, R. Bionta, T. Ma, B. Spears, J. R. Rygg, L. R. Benedetti, R. P. J. Town, D. K. Bradley, E. L. Dewald, D. Fittinghoff, O. S. Jones, H. R. Robey, J. D. Moody, S. Khan, D. A. Callahan, A. Hamza, J. Biener, P. M. Celliers, D. G. Braun, D. J. Erskine, S. T. Prisbrey, R. J. Wallace, B. Kozioziemski, R. Dylla-Spears, J. Sater, G. Collins, E. Storm, W. Hsing, O. Landen, J. L. Atherton, J. D. Lindl, M. J. Edwards, J. A. Frenje, M. Gatu-Johnson, C. K. Li, R. Petrasso, H. Rinderknecht, M. Rosenberg, F. H. Séguin, A. Zylstra, J. P. Knauer, G. Grim, N. Guler, F. Merrill, R. Olson, G. A. Kyrala, J. D. Kilkenny, A. Nikroo, K. Moreno, D. E. Hoover, C. Wild, and E. Werner, Physics of Plasmas **21**, 056318 (2014).
[6] A. L. Kritcher, R. Town, D. Bradley, D. Clark, B. Spears, O. Jones, S. Haan, P. T. Springer, J. Lindl, R. H. H. Scott, D. Callahan, M. J. Edwards, and O. L. Landen, Physics of Plasmas **21**, 042708 (2014).
[7] S. W. Haan, J. D. Lindl, D. A. Callahan, D. S. Clark, J. D. Salmonson, B. A. Hammel, L. J. Atherton, R. C. Cook, M. J. Edwards, S. Glenzer, A. V. Hamza, S. P. Hatchett, M. C. Herrmann, D. E. Hinkel, D. D. Ho, H. Huang, O. S. Jones, J. Kline, G. Kyrala, O. L. Landen, B. J. MacGowan, M. M. Marinak, D. D. Meyerhofer, J. L. Milovich, K. A. Moreno, E. I. Moses, D. H. Munro, A. Nikroo, R. E. Olson, K. Peterson, S. M. Pollaine, J. E. Ralph, H. F. Robey, B. K. Spears, P. T. Springer, L. J. Suter, C. A. Thomas, R. P. Town, R. Vesey, S. V. Weber, H. L. Wilkens, and D. C. Wilson, Physics of Plasmas **18**, 051001 (2011).
[8] J. D. Lindl, P. Amendt, R. L. Berger, S. G. Glendinning, S. H. Glenzer, S. W. Haan, R. L. Kauffman, O. L. Landen, and L. J. Suter, Physics of Plasmas **11**, 339 (2004).
[9] S. Atzeni and J. Meyer-ter-Vehn, *The Physics of Inertial Fusion* (Oxford Science Publications, 2004).
[10] B. A. Hammel, S. W. Haan, D. S. Clark, M. J. Edwards, S. H. Langer, M. M. Marinak, M. V. Patel, J. D. Salmonson, and H. A. Scott, High Energy Density Physics **6**, 171 (2010).
[11] R. D. Richtmyer, Communications on Pure and Applied Mathematics **13**, 297 (1960).
[12] E. E. Meshkov, Fluid Dynamics **4**, 101 (1969).
[13] L. Rayleigh, Proceedings of the London Mathematical Society **s1-14**, 170 (1882).
[14] G. Taylor, Proceedings of the Royal Society of London. Series A. Mathematical and Physical Sciences **201**, 192 (1950).
[15] L. Kelvin, Philosophical Magazine **42**, 362 (1871).
[16] H. von Helmholtz, Monthly Reports of the Royal Prussian Academy of Philosopy in Berlin **23**, 215 (1868).
[17] V. N. Goncharov, O. V. Gotchev, E. Vianello, T. R. Boehly, J. P. Knauer, P. W. McKenty, P. B. Radha, S. P. Regan, T. C. Sangster, S. Skupsky, V. A. Smalyuk, R. Betti, R. L. McCrory, D. D. Meyerhofer, and C. Cherfils-Clérouin, Physics of Plasmas **13**, 012702 (2006).
[18] R. Betti, V. N. Goncharov, R. L. McCrory, and C. P. Verdon, Physics of Plasmas **5**, 1446 (1998).
[19] V. Lobatchev and R. Betti, Phys. Rev. Lett. **85**, 4522 (2000).
[20] M. S. Plesset, Journal of Applied Physics **25**, 96 (1954).
[21] V. N. Goncharov, P. McKenty, S. Skupsky, R. Betti, R. L. McCrory, and C. Cherfils-Clérouin, Physics of Plasmas **7**, 5118 (2000).
[22] J. L. Peterson, D. S. Clark, L. P. Masse, and L. J. Suter, Physics of Plasmas **21**, 092710 (2014).
[23] V. A. Thomas and R. J. Kares, Phys. Rev. Lett. **109**, 075004 (2012).
[24] C. R. Weber, D. S. Clark, A. W. Cook, L. E. Busby, and H. F. Robey, Phys. Rev. E **89**, 053106 (2014).
[25] V. A. Smalyuk, D. T. Casey, D. S. Clark, M. J. Edwards, S. W. Haan, A. Hamza, D. E. Hoover, W. W. Hsing, O. Hurricane, J. D. Kilkenny, J. Kroll, O. L. Landen, A. Moore, A. Nikroo, L. Peterson, K. Raman, B. A. Remington, H. F. Robey, S. V. Weber, and K. Widmann, Physical Review Letters **112**, 185003 (2014).
[26] K. S. Raman, V. A. Smalyuk, D. T. Casey, S. W. Haan, D. E. Hoover, O. A. Hurricane, J. J. Kroll, A. Nikroo, J. L. Peterson, B. A. Remington, H. F. Robey, D. S. Clark, B. A. Hammel, O. L. Landen, M. Marinak, D. H. Munro, K. J. Peterson, and J. D. Salmonson, Physics of Plasmas **21**, 072710 (2014).
[27] D. T. Casey, V. A. Smalyuk, K. Raman, J. L. Peterson, L. B. Hopkins, D. A. Callahan, D. S. Clark, E. L. Dewald, T. R. Dittrich, S. W. Haan, D. E. Hinkel, D. Hoover, O. Hurricane, J. J. Kroll, O. L. Landen, A. Moore, A. Nikroo, H.-S. Park, B. A. Remington, H. F. Robey, J. R. Rygg, J. D. Salmonson, R. Tommasini, and K. Widmann, Physical Review E **90**, 011102(R) (2014).
[28] M. J. Edwards, P. K. Patel, J. D. Lindl, L. J. Atherton, S. H. Glenzer, S. W. Haan, J. D. Kilkenny, O. L. Landen, E. I. Moses, A. Nikroo, R. Petrasso, T. C. Sangster, P. T. Springer, S. Batha, R. Benedetti, L. Bernstein, R. Betti, D. L. Bleuel, T. R. Boehly, D. K. Bradley, J. A. Caggiano, D. A. Callahan, P. M. Celliers, C. J. Cerjan, K. C. Chen, D. S. Clark, G. W. Collins, E. L. Dewald, L. Divol, S. Dixit, T. Doeppner, D. H. Edgell, J. E. Fair, M. Farrell, R. J. Fortner, J. Frenje, M. G. Gatu Johnson, E. Giraldez, V. Y. Glebov, G. Grim, B. A. Hammel, A. V. Hamza, D. R. Harding, S. P. Hatchett, N. Hein, H. W. Herrmann, D. Hicks, D. E. Hinkel, M. Hoppe, W. W. Hsing, N. Izumi, B. Jacoby, O. S. Jones, D. Kalantar, R. Kauffman, J. L. Kline, J. P. Knauer, J. A. Koch, B. J. Kozioziemski, G. Kyrala, K. N. LaFortune, S. L. Pape, R. J. Leeper, R. Lerche, T. Ma, B. J. MacGowan, A. J. MacKinnon, A. Macphee, E. R. Mapoles, M. M. Marinak, M. Mauldin, P. W. McKenty, M. Meezan, P. A. Michel, J. Milovich, J. D. Moody, M. Moran, D. H. Munro, C. L. Olson, K. Opachich, A. E. Pak, T. Parham, H.-S. Park, J. E. Ralph, S. P. Regan, B. Remington, H. Rinderknecht, H. F. Robey, M. Rosen,

S. Ross, J. D. Salmonson, J. Sater, D. H. Schneider, F. H. Séguin, S. M. Sepke, D. A. Shaughnessy, V. A. Smalyuk, B. K. Spears, C. Stoeckl, W. Stoeffl, L. Suter, C. A. Thomas, R. Tommasini, R. P. Town, S. V. Weber, P. J. Wegner, K. Widman, M. Wilke, D. C. Wilson, C. B. Yeamans, and A. Zylstra, Physics of Plasmas **20**, 070501 (2013).

[29]T. R. Dittrich, O. A. Hurricane, D. A. Callahan, E. L. Dewald, T. Döppner, D. E. Hinkel, L. F. Berzak Hopkins, S. Le Pape, T. Ma, J. L. Milovich, J. C. Moreno, P. K. Patel, H.-S. Park, B. A. Remington, J. D. Salmonson, and J. L. Kline, Phys. Rev. Lett. **112**, 055002 (2014).

[30]O. A. Hurricane *et al.*, Nature **505**, 343 (2014).

[31]M. M. Marinak, B. A. Remington, S. V. Weber, R. E. Tipton, S. W. Haan, K. S. Budil, O. L. Landen, J. D. Kilkenny, and R. Wallace, Phys. Rev. Lett. **75**, 3677 (1995).

[32]M. M. Marinak, S. G. Glendinning, R. J. Wallace, B. A. Remington, K. S. Budil, S. W. Haan, R. E. Tipton, and J. D. Kilkenny, Phys. Rev. Lett. **80**, 4426 (1998).

[33]D. S. Clark, D. E. Hinkel, D. C. Eder, O. S. Jones, S. W. Haan, B. A. Hammel, M. M. Marinak, J. L. Milovich, H. F. Robey, L. J. Suter, and R. P. J. Town, Physics of Plasmas **20**, 056318 (2013).

[34]Y. Aglitskiy, M. Karasik, A. L. Velikovich, N. Metzler, S. T. Zalesak, A. J. Schmitt, J. H. Gardner, V. Serlin, J. Weaver, and S. P. Obenschain, Physica Scripta **2008**, 014021 (2008).

[35]D. S. Clark, J. L. Milovich, D. E. Hinkel, J. D. Salmonson, J. L. Peterson, L. F. Berzak Hopkins, D. C. Eder, S. W. Haan, O. S. Jones, M. M. Marinak, H. F. Robey, V. A. Smalyuk, and C. R. Weber, Physics of Plasmas **21**, 112705 (2014).

[36]R. Tommasini, Bull. Am. Phys. Soc. **59**, 237 (2014).